Analysis and Fault Tolerant Control for Dual Three-Phase PMSM based on Virtual Healthy Model

Boyuan Zheng, Jibin Zou, *Senior Member, IEEE*, Bingjun Li, Mi Tang, *Member, IEEE*, Yongxiang Xu, *Member, IEEE*, and Pericle Zanchetta, *Fellow, IEEE*

***Abstract*- Dual three-phase permanent magnet synchronous machines (DTP-PMSMs) are famous for their fault-tolerant capability. However, the complex modeling, high copper loss and torque ripple under post-fault operation limit their further application. In this paper, a fault tolerant control (FTC) strategy is developed for DTP-PMSMs under the open-phase fault (OPF) with straightforward modeling and smooth output torque. The virtual healthy DTP-PMSM model, where the coordinate transformation, the modulation strategy and the controller structure remain unchanged under OPF, is adopted in the proposed FTC scheme. And the current references are derived in sinusoidal waves with minimum copper loss. The inaccurate transmission of control signals under OPF is also focused on. Comprehensive theoretical analysis shows the relationship between the controller output voltage and the actual stator voltage should be considered in the proposed FTC strategy otherwise distortion in torque and current will be introduced. The voltage compensation is utilized to compensate for the voltage difference and ensure the smooth torque output. Besides, a quasi proportional resonance (quasi-PR) controller is designed to further suppress the residual torque ripple. The proposed strategy will not induce complex implementation and heavy computation burden. Simulation and experiment results prove the analysis and the effectiveness of the proposed strategy.**

***Index Terms*- Dual three-phase PMSM, fault tolerant control, modeling, torque ripple suppression, copper loss, voltage constraint.**

NOMENCLATURE

u_s	phase voltage	i_s	phase current
R	stator resistance	L_s	stator inductance
ψ_s	magnetic flux in stationary frame	ψ_{md}	magnetic flux of permanent magnet
P	number of pole pairs	θ	electrical angle
T_e	electromagnetic torque	u_α, u_β, u_{z1}, u_{z2}	phase voltage in α-β, z_1-$z_2$frame
i_α, i_β, i_{z1}, i_{z2}	stator current in α-β, z_1-z_2 frame	L_z	leakage-inductance in z_1-z_2 frame
L_α, L_β, $L_{\alpha\beta}$	inductance in α-β frame	ω	electrical speed
L_d, L_q	self-inductance in d-q frame	i_d,i_q	stator current in d-q frame
L_0	DC component of self-inductance	I_q	DC component of q-axis current
u_{x_c}	the calculated output phase voltage in phase x	u_{x_r}	the real input phase voltage in phase x
u_{xy_c}	the calculated voltage between phase x and y	u_{xy_r}	the real voltage between phase x and y
I_{d2}, I_{q2}	value of 2th harmonic stator current	φ_{d2},φ_{q2}	phase of 2nd harmonic stator current
k_p	proportional element in quasi-PR controller	ω_{pr}	resonance frequency in quasi-PR controller
k_r	resonance coefficient in quasi-PR controller	ω_c	bandwidth of the quasi-PR controller

Corresponding author: Jibin Zou (zoujibin@hit.edu.cn)
Boyuan Zheng is with College of Intelligent Systems Science and Engineering, Harbin Engineering University, Harbin, China (*e-mail:* zhengboyuan_hit@outlook.com).
Jibin Zou, Bingjun Li, Yongxiang Xu are with the School of Electrical Engineering, Harbin Institute of Technology, Harbin, China(*e-mail:* zoujibin@hit.edu.cn, libingjun12138@163.com, xuyx@hit.edu.cn).
Mi Tang, Pericle Zanchetta are with Power Electronics, Machines and Control Group, University of Nottingham, Nottingham, U.K (*email:* mi.tang2@nottingham.ac.uk , pericle.zanchetta@nottingham.ac.uk).
Pericle Zanchetta is also with Department of Electrical, Computer and Biomedical Engineering, University of Pavia, Italy

I. INTRODUCTION

Multiphase Permanent Magnet Synchronous Machines (PMSMs) have drawn more and more attention from the industry and academia due to their advantage in high-power and high-reliability applications compared to their three-phase counterparts. One promising candidate for multiphase machines is the DTP-PMSM. It has two sets of three-phase stator windings spatially shifted by 30 electrical degrees with isolated neutral points. Another advantage of the DTP-PMSM is that it can eliminate the 6th torque harmonic pulsation. These advantages make the DTP-PMSM suitable for applications such as electric vehicles, railways and aircrafts [1, 2].

Reliability is a core requirement in electrical drive systems, especially in more electric aircraft and electric vehicles [3-6]. And the fault tolerant control of PMSMs has been intensively studied to improve the reliability. The focus of this paper is on electrical faults, which mainly include short-circuit faults (SPFs) and OPFs. According to [7], the failure rate of power switches contributes more than half of all the remaining component faults. And for DTP-PMSMs, more power switches mean a higher failure rate. Besides, the SPFs can be converted into the OPFs by reconfiguration, so the OPFs caused by voltage source inverters (VSI) are studied intensively [8-10] and further discussed in this paper.

For the DTP-PMSMs, when one or more phases are under OPFs, the simplest way is to remove the whole faulty three-phase winding and use the other set of three-phase healthy phases for torque production [11, 12]. The torque output is

smooth and the control strategy remains unchanged but this will result in significant torque reduction. The most popular way is to isolate the faulty phase and make use of the remaining phases for torque production [13-15] where the remaining healthy phases are fully utilized. Besides, leveraging the remaining one healthy switch is also studied in [16] for the single open-switch fault while the control scheme remains the same as that under OPF. So this paper also focuses on the strategy in isolating the faulty phase.

The basic requirement of the FTC is to eliminate the torque ripple under post-fault operation. One approach is based on inducing additional hardware. High-reliability inverter topologies can be utilized in FTCs, such as four-leg power converters, multilevel converters and matrix converters [17-19]. Besides, some structures in the winding, such as open-winding configuration, are proposed in [20, 21] to remove the existing current constraints under OPF. However, additional hardware will increase the cost inevitably.

Another approach is optimization-based. This type of methods does not require additional hardware assistance and can fully utilize the inherited advance in multiphase machines. After the OPF occurs, the constraints in the machine system reduce, the machine loses one degree of freedom. And the solutions of the system equations are no more unique. So the design of the FTC strategies is regarded as a design problem with constraints and different optimization targets. The targets include maximum torque, minimum torque ripple and minimum copper loss [22, 23]. In [24], the current references are derived with different winding configurations either in minimum copper loss or maximum torque output. In [9], a hybrid controller is designed to switch between different optimization currents. And non-sinusoidal phase current references are given in [25] to further reduce the copper loss.

Different modeling methods to the OPF machine and various controllers are proposed to achieve the postfault optimization targets. For the modeling strategies, the post-fault DTP-PMSM is regarded as an abnormal five-phase PMSM in [26], while the voltage-current equations in d-q axes are not fully decoupled in the post-fault model and the space vector modulation strategy also needs reconstruction. The DTP-PMSM with single-phase OPF is considered as a healthy three-phase PMSM and a two-phase PMSM in [27]. In [24], the normal (i.e., not a reduced-order) decoupling transformation is utilized in the postfault operation and the machine with OPF is regarded as a 'virtual healthy model'. The advantage of this modeling method is that the same voltage equations based on healthy decoupling equations can still be used under postfault operations, as well as the modulation strategy and the controller. The coupling in currents based on the virtual healthy model are discussed in [28, 29]. But harmonics in torque and phase current distortion still exists under the FTC strategy because of the inaccurate transmission of control signals in the faulty phase.

As for the controllers, iterative learning algorithm [30] and LaGrange equation-based controller [31] are designed to solve the optimization problem under postfault operations. A method based on genetic algorithm (GA) is proposed in [32] for the FTC of interior PMSMs. While these methods involve a heavy burden to the controllers. A look-up table is developed to avoid online computation but it proposes a high demand for the memories [32]. Model predictive controller is also utilized in a five-phase PMSM [33] or DTP-PMSMs [13] under OPF with additional constraints on cost functions. And deadbeat controller is utilized to trace the non-DC current references, either sinusoidal [16] or non-sinusoidal [25] in FTC strategies. While the performance of the controllers heavily relies on the predictive model and accuracy of the machine parameters. To reduce the effect of the inaccurate control signal transmission under postfault operation, high bandwidth controllers are utilized [24]. But the voltage difference in the faulty phase still exists under postfault operation and the relative control signal transmission is still inaccurate. Therefore, it only suppresses the influence of the voltage difference by increasing the gain of the controller. In addition, the use of relatively different control algorithms under normal operation and fault-tolerant states will also increase the complexity of the system and reduce the reliability of the system.

The antiparallel diodes of the faulty phase have been considered in recent research [34, 35]. When the OPFs occur, the power switches in the faulty phase are shut down to achieve open-circuit situation. In most cases, it is achieved by software rather than disconnecting the faulty phase from the inverter physically. But shutting down the power switches in the faulty phases by software do not create the desired open-circuit situation because of current path provided by the antiparallel diodes. There is still insufficient research on the effect of this freewheeling current in the postfault operation.

This paper aims to propose a FTC strategy based on the virtual healthy model in which the modeling and the controller of the DTP-PMSM do not need to change significantly after the OPF to increase reliability. The difference between the controller output voltage and the actual stator voltage is also theoretically derived under OPF to solve the the problem of the control signal transmission inaccuracy. Its effects are eliminated by voltage compensation and quasi-PR controller in the proposed FTC strategy to provide smooth output torque. The antiparallel diode of the faulty phase is considered as well.

The rest of this paper is organized as follows. The mathematical modeling and control strategy based on vector space decomposition (VSD) of a healthy DTP-PMSM are briefly introduced in Section II. The virtual healthy model to the DTP-PMSM under OPF is discussed and the sinusoidal current references with minimized copper loss are given in Section III. Section IV gives a comprehensive analysis of the torque ripple and current distortion caused by the voltage difference between the controller and the windings. Based on the analysis above, in Section V, the proposed FTC strategy based on the virtual healthy model is developed. Voltage compensation is utilized in the proposed scheme and the residual harmonics are suppressed by the quasi-PR controller. Simulation and experimental results are given in Section VI and conclusions are made in Section VII.

II. Operation Principle of DTP-PMSM and Conventional Control Schemes

A. Modeling of the DTP- PMSM under healthy operation

A simple but precise model is essential for the analysis and control. The DTP-PMSM discussed in this paper has two sets of three-phase windings with 30 electrical degree shift. The neutral points of the two windings are disconnected, as shown in Fig.1. The magnetic saturation effect is neglected and parameters in each phase are the same to simplify the analysis.

The voltage equation of DTP-PMSMs can be expressed as (1) and the flux equation can be given as (2) in the stationary frame. And the torque equation can be calculated as (3) based on the virtual displacement.

$$\begin{aligned} u_s &= R_s i_s + \frac{d\psi_s}{dt} \\ u_s &= \begin{bmatrix} u_a & u_b & u_c & u_{a1} & u_{b1} & u_{c1} \end{bmatrix}^T \\ i_s &= \begin{bmatrix} i_a & i_b & i_c & i_{a1} & i_{b1} & i_{c1} \end{bmatrix}^T \\ \psi_s &= L_s i_s + \gamma_s \psi_{md} \end{aligned} \tag{1}$$

$$\begin{aligned} \gamma_s &= \begin{bmatrix} \cos\theta & \cos(\theta_1) & \cos(\theta_2) & \cos(\theta_3) & \cos(\theta_4) & \cos(\theta_5) \end{bmatrix}^T \\ \theta_1 &= \theta - \frac{2\pi}{3}, \theta_2 = \theta + \frac{2\pi}{3}, \theta_3 = \theta - \frac{\pi}{6}, \theta_4 = \theta - \frac{5\pi}{6}, \theta_5 = \theta + \frac{\pi}{2} \end{aligned} \tag{2}$$

$$T_e = P\left(\frac{1}{2} i_s^T \frac{\partial L_s}{\partial \theta} i_s + i_s^T \frac{\partial \gamma_s}{\partial \theta} \psi_{md}\right) \tag{3}$$

The analysis and control in the stationary frame are complex because of the coupled matrix of inductance. In dual-three phase machines, the conventional decoupling method is not effective anymore. The dual d-q axes decomposition strategy [36] or the VSD strategy can be applied and the VSD strategy can achieve complete decomposition. The transformation matrix from the original stationary coordinate system (ABC, $A_1B_1C_1$) to the 2-phase stationary coordinate system (α-β, z_1-z_2) is shown in (4) according to [36]. The voltage equation in this coordinate system is shown in (5).

$$T_{abc-\alpha\beta} = \frac{1}{3} * \begin{bmatrix} 1 & -\frac{1}{2} & -\frac{1}{2} & \frac{\sqrt{3}}{2} & -\frac{\sqrt{3}}{2} & 0 \\ 0 & \frac{\sqrt{3}}{2} & -\frac{\sqrt{3}}{2} & \frac{1}{2} & \frac{1}{2} & -1 \\ 1 & -\frac{1}{2} & -\frac{1}{2} & -\frac{\sqrt{3}}{2} & \frac{\sqrt{3}}{2} & 0 \\ 0 & -\frac{\sqrt{3}}{2} & \frac{\sqrt{3}}{2} & \frac{1}{2} & \frac{1}{2} & -1 \\ 1 & 1 & 1 & 0 & 0 & 0 \\ 0 & 0 & 0 & 1 & 1 & 1 \end{bmatrix} \tag{4}$$

$$\begin{bmatrix} u_\alpha \\ u_\beta \\ u_{z1} \\ u_{z2} \end{bmatrix} = \begin{bmatrix} R + L_\alpha \frac{d}{dt} & L_{\alpha\beta} \frac{d}{dt} & 0 & 0 \\ L_{\alpha\beta} \frac{d}{dt} & R + L_\beta \frac{d}{dt} & 0 & 0 \\ 0 & 0 & R + L_z \frac{d}{dt} & 0 \\ 0 & 0 & 0 & R + L_z \frac{d}{dt} \end{bmatrix} \begin{bmatrix} i_\alpha \\ i_\beta \\ i_{z1} \\ i_{z2} \end{bmatrix} + \psi_{md} \frac{d}{dt} \begin{bmatrix} \cos\theta \\ \sin\theta \\ 0 \\ 0 \end{bmatrix} \tag{5}$$

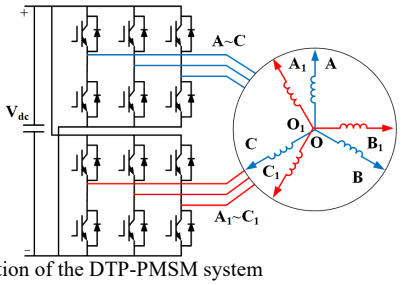

Fig.1 Configuration of the DTP-PMSM system

It is only necessary to transform the α-β components into the synchronous reference frame since only the α-β axes are related to the energy conversion. And the transform matrix is the same as that in three-phase PMSMs. The corresponding torque equation in DTP-PMSMs is shown in (6) in the synchronous reference frame.

$$T_e = 3P\left[\left(L_d - L_q\right) i_d i_q + i_q \psi_{md}\right] \tag{6}$$

B. Control Framework

The ordinary control schemes of the DTP-PMSM under healthy operations include the two-dimensional vector control and four-dimensional vector control [37]. The two-dimensional vector control only controls the current in d-q subspace which is related to the energy conversion. The reference voltages in z_1-z_2 subspace are given as zero to suppress the harmonic current. But current harmonics still exist due to the low-impedance characteristics in z_1-z_2 subspace. Another strategy is the four-dimensional vector control. It suppresses the harmonic current in z_1-z_2 subspace with close-loops. Nevertheless, it is more difficult to implement. A brief control topology can be shown in Fig.2. And three-phase decomposition space vector pulse width modulation (SVPWM) with two identical three-phase SVPWM modules, is used as the modulation strategy.

III. Modeling of the DTP-PMSM with Open-Phase Fault Based on Virtual Healthy Model

In previous FTC schemes, when the one-phase OPF occurs, the post-fault machine is usually considered as an abnormal five phase machine, as shown in Fig.3 (a), or regard it as a

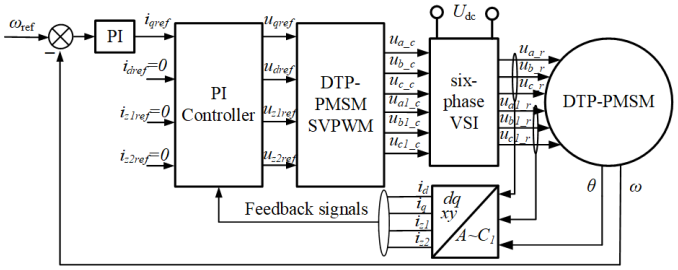

Fig.2 Control diagram of the DTP-PMSM system under normal operation

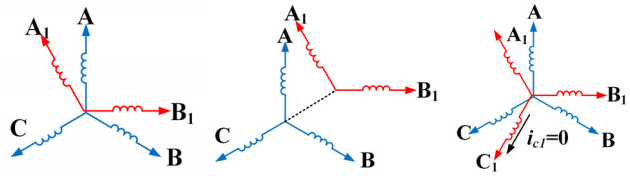

(a) (b) (c)

Fig.3 different modeling strategies under OPF

combination of a healthy 3-phase machine and a 2-phase machine, as shown in Fig.3(b). The postfault model of the machine, specifically, the voltage-current equation, need to be redesigned according to the winding arrangement of this abnormal machine[26, 27]. The control and modulation strategies shown in Fig.2 might not be applicable under these modeling schemes. Thus, large modification is induced when switching to postfault operation, which will reduce the system reliability and bring heavy burden to the controller.

To minimize the changes in modeling and control, the DTP-PMSM with one-phase OPF is treated as a virtual healthy model in this paper and the corresponding phase current becomes zero under OPF, as shown in Fig.3(c). It is assumed that the OPF occurs in the VSI and the windings is not damaged. In this postfault model, the uniform decomposition matrix, control framework and SVPWM strategy under healthy state are also applicable under open-phase fault.

As for the machine equations in the virtual healthy model under OPF, (4) and (5) remain the same since the winding is not physically broken. And the effect of OPF is mainly on the currents. The open-phase fault in phase C_1 is considered in the following analysis procedure. The situations that the open-phase fault occurs in other phases can be equivalent to this situation by rotating.

Substituting i_{c1}=0 into (4) and combining with Kirchhoff's current law, (8) can be derived,

$$\begin{bmatrix} i_{\alpha\_f} \\ i_{\beta\_f} \\ i_{z1\_f} \\ i_{z2\_f} \\ 0 \\ 0 \end{bmatrix} = \mathrm{T}_{abc-\alpha\beta} \begin{bmatrix} i_{a\_f} \\ i_{b\_f} \\ -i_{a\_f}-i_{b\_f} \\ i_{a1\_f} \\ -i_{a1\_f} \\ 0 \end{bmatrix} = \begin{bmatrix} \frac{i_{a\_f}}{2}+\frac{\sqrt{3}}{3}i_{a1\_f} \\ \frac{\sqrt{3}}{6}i_{a\_f}+\frac{\sqrt{3}}{3}i_{b\_f} \\ \frac{i_{a\_f}}{2}-\frac{\sqrt{3}}{3}i_{a1\_f} \\ -(\frac{\sqrt{3}}{6}i_{a\_f}+\frac{\sqrt{3}}{3}i_{b\_f}) \\ 0 \\ 0 \end{bmatrix} \tag{8}$$

where the subscript '_f' indicates the quantity under the postfault operation. According to (8), after the single-phase OPF in phase C_1 occurs, the number of the independent phase current decreases from four to three, indicating that the DTP-PMSM under one-phase OPF is reduced from a fourth-order system to a third-order system under postfault operation. It is also valid in the 2-phase stationary coordinate system (α-β, z_1-z_2). The current in β-axis and z_2-axis are no longer decoupled anymore and i_{z2} is decided by i_β, with i_{z2}=- i_β. So the post-fault voltage-current equations in α, β, z_1 axis are the same with (5) and z_2-axis equations can be shown in (9).

$$u_{z2} = -Ri_\beta - L_z\frac{di_\beta}{dt} \tag{9}$$

As for the torque equation, since the windings of the machine remain the same, the inductance matrix remains the same after OPF. Currents in z_1-z_2 subspace have no contribution to energy conversion, so the torque equation has the same form as that in (6).

The current references under OPF are derived then. The optimization target in this paper is to achieve the same torque output with minimum copper loss. Since the torque is constant under postfault operation and a surface-mounted DTP-PMSM is studied in this paper, according to (6), the q-axis current should be the same after the OPF, that is, I_q*. The d-axis current and z_1-axis current will give no contribution to torque production and they should be suppressed to zero to achieve the minimum copper loss. As for the reference in z_2-axis current, it will be decided by i_β. So it will be determined once the references in α, β, z_1 axis are determined and it is not controllable. The current references with OPF in phase C_1 are shown in (10) where the superscript * indicates the current reference values.

$$\begin{cases} i^*_{\alpha\_f} = -I^*_q\sin\theta \\ i^*_{\beta\_f} = I^*_q\cos\theta \\ i^*_{z1\_f} = 0 \\ i^*_{z2\_f} = -I^*_q\cos\theta \end{cases} \tag{10}$$

The phase currents are optimized as sine waves to be suitable for vector control. According to (8), the amplitude and phase of the reference currents in phase A, phase B and phase A_1, that is 6 unknown coefficients, need to be solved. Substituting (8) into (10), the phase current references should satisfy (11).

$$\begin{cases} \frac{I_{a\_f}}{2}\cos(\theta+\varphi_a)+\frac{\sqrt{3}I_{a1\_f}}{3}\cos(\theta+\varphi_{a1}) = -I^*_q\sin\theta \\ \frac{\sqrt{3}I_{a1\_f}}{6}\cos(\theta+\varphi_{a1})+\frac{\sqrt{3}I_{b\_f}}{3}\cos(\theta+\varphi_b) = I^*_q\cos\theta \\ \frac{I_{a\_f}}{2}\cos(\theta+\varphi_a)+\frac{\sqrt{3}I_{a1\_f}}{3}\cos(\theta+\varphi_{a1}) = 0 \end{cases} \tag{11}$$

where $I_{X\_f}\cos(\theta+\varphi_X)$ represents the unsolved phase current, I_{X_f} represents the amplitude and φ_X represents the relevant phase. Since (11) should hold for all θ, six equations can be derived from (11) and all the 6 unknown coefficients can be solved. And the corresponding current references should be,

$$\begin{cases} i^*_{a\_f} = I^*_q\cos(\theta+\frac{\pi}{2}) \\ i^*_{b\_f} = \frac{\sqrt{13}}{2}I^*_q\cos(\theta+\varphi_b), \tan\varphi_b = -\frac{\sqrt{3}}{6} \\ i^*_{c\_f} = \frac{\sqrt{13}}{2}I^*_q\cos(\theta+\varphi_c), \tan\varphi_c = \frac{\sqrt{3}}{6} \\ i^*_{a1\_f} = \frac{\sqrt{3}}{2}I^*_q\cos(\theta+\frac{\pi}{2}) \\ i^*_{b1\_f} = -\frac{\sqrt{3}}{2}I^*_q\cos(\theta+\frac{\pi}{2}) \\ i^*_{c1\_f} = 0 \end{cases} \tag{12}$$

IV. Effect of the Voltage Difference in Virtual Healthy Model-based FTC Strategy

The FTC strategy can be designed based on the current references as shown in (12). But for the FTC strategy based on

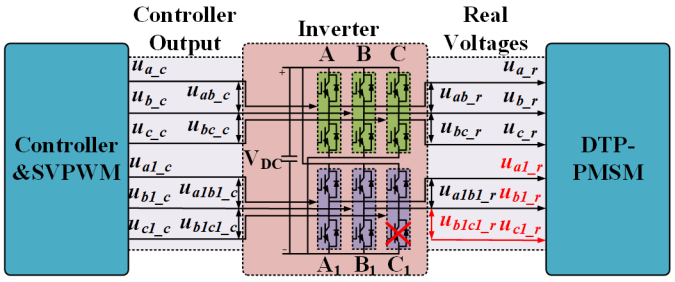

Fig.4 Relationship of the controller output voltages and real voltages with OPF in phase C_1

the virtual healthy model, the current relationship above is not the only thing that needs to be considered. Due to the OPF in the inverter, the control signals, that is, the voltage components, cannot be accurately transmitted to the windings of the DTP-PMSM as well. And the main purpose of this part is to find out the voltage difference, Δu_{c1}, between the real winding voltage of phase C_1, u_{c1_r}, and the controller output voltage of phase C_1, u_{c1_c}, as shown in Fig.4 under OPF caused by the inverter and to calculate the harmonic current and torque ripple caused by Δu_{c1}, where the subscript '_c' represents the controller output voltage signals and subscript '_r' represents the real winding voltages.

Most of the existing FTC strategies consider only the constraint in currents. While after an OPF occurs, in the actual model, the control signal of the faulty phase cannot be accurately transmitted to the motor due to the shutting down of the faulty inverter, so there is also a voltage difference. It will not affect the FTC strategies based on the abnormal five phase machine model since there is no control signal to the faulty phase but it will surely cause the control performance distortion based on the virtual healthy model. Some advance controllers are proposed [16] to suppress its effect with the high-bandwidth characteristics. While this will bring extra memory or calculation burden to the CPU and the effect of the voltage difference still exists. So this part establishes the mathematical model of the voltage difference and its effect.

Firstly, the actual winding voltage of the faulty phase C_1 should be solved. The winding voltages are u_{a_r}~u_{c1_r} as shown in Fig.4. Since the windings are healthy under the OPF fault, the voltage in phase C_1 is not zero. Specifically, u_{c1_r} is equal to the back electromotive force (EMF) because of the rotation. According to the voltage-current equation as shown in (1), the relationship of the phase voltages in A_1, B_1, C_1 can be derived as (13).

$$u_{a1\_r}+u_{b1\_r}+u_{c1\_r}=0 \tag{13}$$

According to (13) and the voltage-current equation as shown in (1), the terminal phase voltage in phase C_1 is,

$$\begin{aligned} u_{c1\_r} &= -u_{a1\_r}-u_{b1\_r} \\ &= -R(i_{a1\_r}+i_{b1\_r})-\frac{d}{dt}(\psi_{a1}+\psi_{b1}) \\ &= -\frac{d}{dt}(\psi_{a1}+\psi_{b1}) \end{aligned} \tag{14}$$

and the flux components can be further expressed as,

$$\begin{aligned} u_{c1\_r} &= -\frac{d}{dt}[L_z(i_{a1}+i_{b1})+\frac{\sqrt{3}}{2}L_0(i_b-i_c) \\ &\quad +(\cos(\theta-\frac{\pi}{6})+\cos(\theta-\frac{5\pi}{6}))\psi_{md}] \\ &= -\frac{\sqrt{3}}{2}L_0\frac{d}{dt}(i_b-i_c)-\psi_{md}\cos\theta \end{aligned} \tag{15}$$

L_0 is equal to L_d for surface-mounted PMSM. And (16) is proposed to replace the differential part on the right side of (15).

$$\begin{aligned} u_{bc\_r} &= R(i_b-i_c)+\frac{d}{dt}(\psi_b-\psi_c) \\ &= R(i_b-i_c)+(\frac{3}{2}L_0+L_z)\frac{d}{dt}(i_b-i_c)+\sqrt{3}\psi_{md}\cos\theta \end{aligned} \tag{16}$$

Substituting (16) into (15), the actual winding voltage of DTP-PMSM on phase C_1 is shown in (17), where the leakage inductance is neglected.

$$u_{c1\_r}=-\frac{\sqrt{3}}{3}[u_{bc\_r}-R(i_b-i_c)] \tag{17}$$

Secondly, the function of the inverter is discussed. It aims to transmit the phase-to-phase voltages, u_{ab_c}~u_{b1c1_c}, from the controller output, to the machine winding. According to Fig.4, after the OPF in phase C_1, since the remaining 5 phases are not affected, the phase-to-phase voltages among phase A~B_1, that is, u_{ab}, u_{bc}, u_{a1b1} remain unchanged in postfault operations after passing the inverter. But u_{b1c1_c} is not equal to u_{b1c1_r} anymore due to the OPF. It is also worth mentioning that only phase-to-phase voltages are transmitted through the inverter, not the phase voltages, and u_{a1_c}, u_{b1_c} are also not equal to u_{a1_r}, u_{b1_r} because of the change in neutral point voltage under OPF.

Then, the controller output voltage of the faulty phase, u_{c1_c}, is derived. u_{α_c}, u_{β_c}, u_{z1_c}, u_{z2_c} are calculated by the FTC scheme which is designed based on voltage-current equations shown in (5) and (9). Then the controller output voltages, u_{a_c}~u_{c1_c} are derived through SVPWM. Since the virtual healthy model is utilized, the modulation strategy remains the same under post-fault operation. The relationship in (4) still holds after the OPF because of the virtual healthy model. And the voltages are written in the form of line voltages instead of phase voltages, as shown in (18), to eliminate the influence of the neutral point voltage.

$$\begin{bmatrix} u_{\alpha\_c} \\ u_{\beta\_c} \\ u_{z1\_c} \\ u_{z2\_c} \end{bmatrix} = \frac{1}{6}\begin{bmatrix} 2u_{ab\_c}+u_{bc\_c}+\sqrt{3}u_{a1b1\_c} \\ \sqrt{3}u_{bc\_c}+u_{a1b1\_c}-2u_{b1c1\_c} \\ 2u_{ab\_c}+u_{bc\_c}-\sqrt{3}u_{a1b1\_c} \\ -\sqrt{3}u_{bc\_c}+u_{a1b1\_c}-2u_{b1c1\_c} \end{bmatrix} \tag{18}$$

And (13) still founds on the controller after substituting "_r" with "_c". To derive the controller output voltage in phase C_1, substituting that into (18), the relationship is shown in (19).

$$\begin{bmatrix} u_{\alpha\_c} \\ u_{\beta\_c} \\ u_{z1\_c} \\ u_{z2\_c} \end{bmatrix} = \frac{1}{6}\begin{bmatrix} 2u_{ab\_c}+u_{bc\_c}+\sqrt{3}u_{a1b1\_c} \\ \sqrt{3}u_{bc\_c}-3u_{c1\_c} \\ 2u_{ab\_c}+u_{bc\_c}-\sqrt{3}u_{a1b1\_c} \\ -\sqrt{3}u_{bc\_c}-3u_{c1\_c} \end{bmatrix} \tag{19}$$

And the controller output voltage on phase C_1 can be expressed as (20) based on (19).

$$u_{c1\_c} = -2u_{z2ref} - \frac{\sqrt{3}}{3}u_{bc\_in} \tag{20}$$

The voltage difference on the faulty phase C_1 can finally be derived by subtracting (20) from (17). Since the z_2-axis current is dependent on β-axis current and cannot be controlled according to (9), u_{z2ref} could be chosen as 0 [38]. The expression of Δu_{c1} is shown in (21).

$$\Delta u_{c1} = u_{c1\_r} - u_{c1\_c} = 2Ri_\beta = 2RI_q\cos\theta \tag{21}$$

Equation (21) can be explained as follows. If the controller output voltages, u_{a_c}~u_{c1_c}, can be transmitted to the windings of the DTP-PMSM without error, the FTC performance would be ideal. But due to the existence of OPF, the actual winding voltages in phase C_1 will change to u_{c1_c}+ Δu_{c1}. It will always exist and cannot be compensated simply by the closed-loop, degrading the control performance.

The following part discusses the effect of the voltage difference on the postfault DTP-PMSM. Due to the virtual healthy model, (19) still founds by substituting "_c" with "_r". So Δu_{c1} will not affect the voltages in α and z_1 axes since voltages in these axes will not be affected by phase C_1. While the voltages in β and z_2 axes are affected. The relationship between the real voltage on the postfault DTP-PMSM and the controller output voltage is shown in (22) by substituting (21) into (19).

$$\begin{bmatrix} u_{\alpha\_r} \\ u_{\beta\_r} \\ u_{z1\_r} \\ u_{z2\_r} \end{bmatrix} = \begin{bmatrix} u_{\alpha\_c} \\ u_{\beta\_c} - I_qR\cos\theta \\ u_{z1\_c} \\ u_{z2\_c} - I_qR\cos\theta \end{bmatrix} \tag{22}$$

And the influence on d-q axes is shown as (23).

$$\begin{cases} \Delta u_{d\_r} = -\dfrac{I_qR}{2}\sin 2\theta \\ \Delta u_{q\_r} = -\dfrac{I_qR}{2}(\cos 2\theta + 1) \end{cases} \tag{23}$$

According to (23), the distortion caused by the voltage constraint on the *d-q* axes is the form of sine waves and the frequency is twice the electrical angle frequency. It will cause the 2nd harmonic currents on the d-q axes current and torque ripple, where the d-q axes current can be expressed in (24) under $i_d=0$ control. In the original stationary coordinate system, the 3rd harmonic current components will also be induced.

$$\begin{cases} i_d = I_{d2}\cos(2\theta + \phi_{d2}) \\ i_q = I_q + I_{q2}\cos(2\theta + \phi_{q2}) \end{cases} \tag{24}$$

Since the DC components of the d-q axes current remain the same due to the same torque, when neglecting the coupling term [39], the amplitude and phase of the 2nd harmonic components in d-q axes can be solved by the voltage-current equations, as shown in (25) and (26), respectively.

$$\begin{cases} I_{d2} = \dfrac{I_qR}{2\sqrt{R^2 + (2\omega L_d)^2}} \\ I_{q2} = \dfrac{I_qR}{2\sqrt{R^2 + (2\omega L_q)^2}} \end{cases} \tag{25}$$

$$\begin{cases} \phi_{d2} = \tan^{-1}(\dfrac{2\omega L_d}{R}) + \dfrac{\pi}{2} \\ \phi_{q2} = \tan^{-1}(\dfrac{2\omega L_q}{R}) + \pi \end{cases} \tag{26}$$

According to (6), the torque ripple induced by the voltage difference can be shown in (27)

$$T_e = 3p_n \begin{bmatrix} \left(L_d - L_q\right)I_{d2}I_{q2}\dfrac{\cos(\phi_{q2} - \phi_{d2})}{2} \\ +I_{q2}\psi_{md}\cos(2\theta - \phi_{q2}) \\ +\left(L_d - L_q\right)I_{d2}I_{q2}\dfrac{\cos(4\theta - \phi_{q2} - \phi_{d2})}{2} \end{bmatrix} \tag{27}$$

So, the voltage difference will cause current distortion and induce torque ripple. To salient DTP-PMSMs, according to (27), for a fixed load, the value of the q-axis current will change and it will also induce 2nd and 4th torque ripple components. To surface DTP-PMSMs, L_d=L_q, only the 2nd torque ripple component is induced.

V. Proposed Fault Tolerant Scheme based on Virtual Healthy Model

Based on the analysis above, the FTC strategies based on the virtual healthy model have the advantages of easy implementation and reduced burden on the CPU. While the voltage difference caused by OPF needs to be considered in the FTC scheme with the virtual healthy model. It will make the control voltage signals unable to be accurately transmitted to the terminals of the DTP-PMSM, inducing extra 2nd harmonic currents and relevant torque ripple which will degrade the control performance and is unneglectable. So this part aims to suppress the induced harmonic current and torque ripple without significantly changing the controller under healthy operation.

A. Basic Control Structure of FTC under OPF

Since the virtual healthy model is utilized, according to the analysis in Section III, the basic control scheme can remain the same as the healthy one with Proportional Integral (PI) controllers in *d*-axis, *q*-axis and z_1-axis. As for the z_2-axis, according to (9), it cannot be controlled independently. And the actual voltage and current on z_2 axis will be decided if the components in *d*, *q*, z_1 axes are well-controlled. So the close-loop current controller on z_2-axis is canceled in the proposed scheme to avoid interference. And u_{z2ref} is directly given in open-loop by the proposed controller.

The topology of the proposed FTC strategy is shown in Fig.5. after the OPF, the three-phase decomposition is utilized as the modulation strategy. Compared to Fig.2, the basic structure of the controller before and after the OPF remains the same with traditional PI controllers. In the proposed FTC scheme, only three current loops are adopted. It matches the

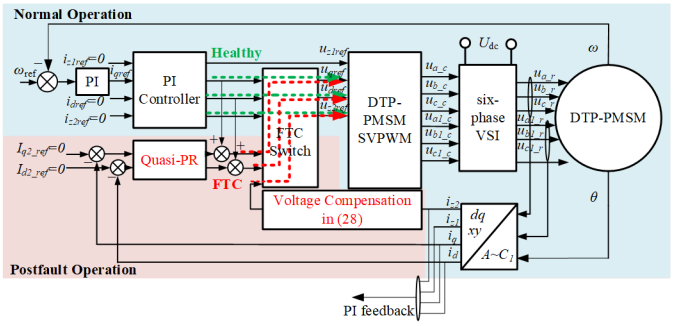

Fig.5 Control diagram of the DTP-PMSM system under normal operation and postfault operation with proposed FTC scheme

analysis that the order of the DTP-PMSM system under one-phase OPF is reduced from 4 to 3. So, in theory, it is enough to control this 3rd-order postfault system with 3 closed loops.

B. Voltage Compensation in the Proposed FTC Scheme

According to the analysis in Section IV, the OPF will interfere with the transmission of the controller output voltages, which will cause the voltage difference in the faulty phase, C_1, thus introducing distortion.

If the voltage difference in phase C_1 is compensated under OPF, the controller output phase voltage can be equal to the actual voltage, that is, $\Delta u_{c1}=0$. Then the control signals can be transmitted to the motor terminals without error, thereby ensuring the control performance under OPF. So the aim of the controller is to choose a suitable value of u_{c1_c} to make Δu_{c1} equal to 0. According to (20), the controller output in phase C_1 is decided by the phase-to-phase voltage between B, C and the reference voltage of z_2 axis. The former one will affect the postfault operation of DTP-PMSM so u_{bc} should not be revised. Since the current in z_2-axis is uncontrollable, choosing different u_{z2ref} will not influence the current of the motor. Thus, it will not interfere with the postfault operation.

Based on (17), (20) and (21), when u_{z2ref} is chosen according to (28), the voltage difference between the controller and the winding terminals in phase C_1 can be compensated.

$$u_{z2ref} = -\frac{\sqrt{3}}{6}R(i_b - i_c) = -Ri_\beta \tag{28}$$

The relevant voltage compensation part is also shown in Fig.5. To further simplify the postfault operation of the controller, i_β in (28) can be replaced by $-i_{z2}$ according to (8). After the OPF is detected, it is only necessary to change the PI controller in z_2-axis to a certain gain to compensate for the voltage constraint.

C. Residual Harmonic Suppression based on quasi-PR controller

According to (17), the actual winding voltage of DTP-PMSM on phase C_1 is achieved by neglecting the leakage-related voltage, $L_z d(i_B-i_C)/dt$. And the voltage difference will also be affected by that. Since the leakage inductance is usually small, this voltage can be ignored as shown in (17). But if the current frequency is high or there's a high requirement for the postfault operation, the leakage-inductance-caused voltage needs to be considered. Since this term contains a differential operation, it is not suitable to compensate this item with feedforward control as shown in (28) since it might reduce the system robustness.

The voltage difference caused by the leakage inductance has the same frequency as the one caused by the resistance. So 2nd-order harmonic currents are induced based on (24). The quasi-PR controller [40] or multiple reference frame (MRF) controller [41] can be utilized to suppress these 2nd order harmonics while the latter one will induce more calculation burden so in this article, the quasi-PR controller is used to suppress the induced harmonics components. Compared to the traditional PR controller, the quasi-PR controller has a limited gain at the resonant frequency with a wider and controllable bandwidth, thus more robust. The transfer function of the quasi-PR controller is shown in (29). And the bode diagram is shown in Fig.6 with different ω_c and k_r.

$$G_{Quasi-PR} = k_p + \frac{k_r \omega_c s}{s^2 + 2\omega_c s + \omega_{pr}^2} \tag{29}$$

The resonant frequency is chosen as 100Hz in the bode diagram. According to Fig.6, the quasi-PR controller is more robust and avoids inducing resonance to the system because of its adjustable bandwidth compared to the traditional one. Besides, since most of the distortion can be suppressed by the voltage compensation shown in (28), the burden of the quasi-PR controller is small and a smaller resonant gain, k_r, can be chosen to improve the robustness of the system. The resonant frequency of the harmonic currents changes with the speed. In the implementation progress, in order to meet the requirement of harmonic suppression at different speed conditions, the resonance frequency ω_{pr} is derived by the feedback speed.

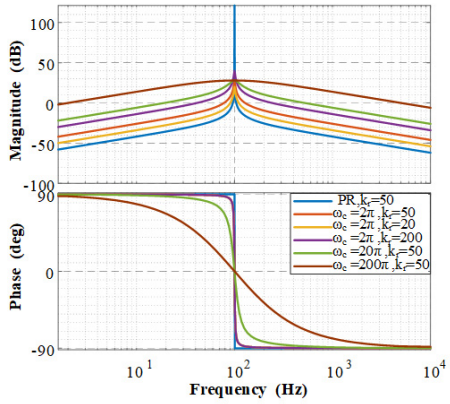

Fig.6 Bode Diagrams of the quasi-PR controller

The d-q axes current obtained by the coordinate transformation of the measured current can be directly used as the feedback of the PI and quasi-PR controller in the proposed scheme as the quasi-PR controller will not affect the DC components. The proposed FTC including quasi-PR controller is also shown in Fig.5. According to Fig.5, the references of the quasi-PR controllers are set as 0 to suppress the induced 2nd harmonics current components by tuning the bandwidth, ω_c, and resonant gain, k_r. The controller output voltages are added by the DC component output from the PI controller and the 2nd harmonic output from the quasi-PR controller.

D. Transfer function and stability analysis

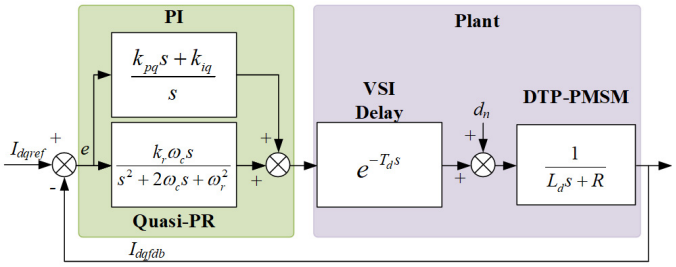

Fig.7 Block diagram of the current control loop in d-q axes

Inducing the quasi-PR controller in the proposed FTC scheme will increase the order of the system and decrease the stability margin. Apart from the coupling in the d-q axes, the block diagram of the current loop of the proposed FTC scheme in d-q axes is shown in Fig.7.

And the transfer function from the reference to the current feedback in Fig.7 is derived in (30).

$$\frac{I_{fdb}}{I_{ref}}=\frac{A}{L_d s^4+(2\omega_c L_d+R)s^3+2R\omega_c s^2+\omega_r^2 L_d s+\omega_r^2 R+A} \tag{30}$$
$$A=[k(s^2+2\omega_c s+\omega_r^2)(L_d s+R)+k_r\omega_c s]e^{-T_d s}$$

where k_{pq}, k_{iq} are the total proportional gain and integral gain of the controller in d-q axes, T_d is the delay time, and $k=k_p/L_d$.

According to the bode diagram and the transfer function, the Nyquist diagram is used to analysis the stability of the controller [41]. The effects of the resonant parameters, k_r, ω_c and the working frequency, ω_r on the stability are needed to be discussed. The other parameters are shown in Table I and the delay time is chosen as 100μs. When the prototype operates at 600rpm, the Nyquist diagram of the system in Fig.7 with different resonant gain, k_r, and bandwidth, ω_c is shown in Fig.8(a)(b). According to the Nyquist diagram, the current loop could keep stable with different k_r and ω_c. Specifically, the stability margin decreases with the k_r and ω_c increasing.

The stability of the proposed controller is also tested at

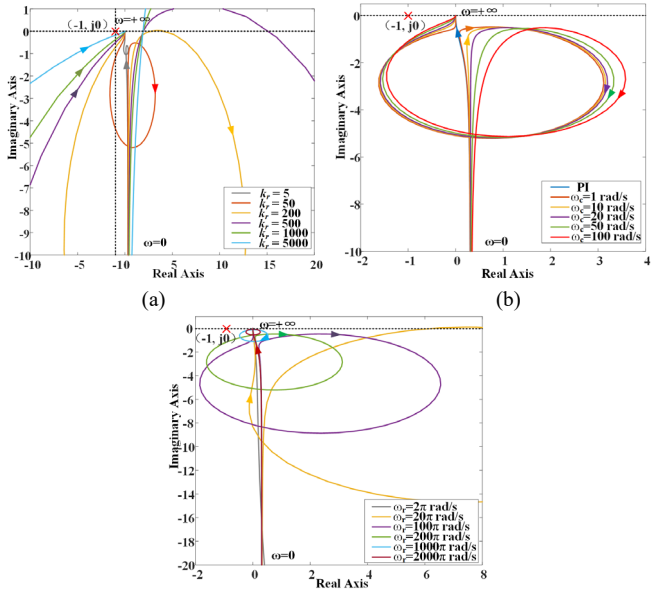

(a) (b) (c)

Fig.8 Nyquist diagram of the current control loop with different k_r, ω_c and ω_r. (a) k_r (b) ω_c (c) ω_r

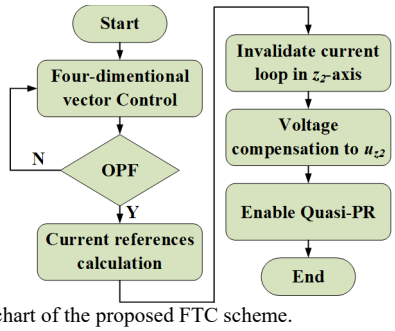

Fig.9 The flowchart of the proposed FTC scheme.

different operation points. the Nyquist diagram with different working frequency, ω_r is shown in Fig.8(c). The system is also stable at different resonant frequencies. As ω_c increasing, the stability margin will decrease first and then increase.

According to the analysis above, the proposed controller will keep stable under different speed and different parameters of the controller.

Fig.9 gives the flowchart of the implementation of the proposed FTC scheme. The current references calculation is based on Section III. The proposed FTC scheme has the same PI controller in *d*, *q*, z_1 axes and SVPWM strategy as the healthy one as shown in Fig.5. As for the current loop in z_2 axis, it is replaced with feedforward voltage compensation to compensate for the voltage difference in the faulty phase. To further suppress the residual 2nd harmonic caused by the leakage inductance, the quasi-PR controller is utilized in d-q axes in the proposed FTC scheme. The proposed FTC scheme maintains the advantage of the virtual healthy model. It will also not increase the calculation burden of the CPU thus it doesn't induce any iterative calculation and good transient response can be expected.

VI. Simulation and Experimental Verification

A. *Experimental Setup*

A surface-mounted DTP-PMSM prototype is used to verify the effectiveness of the analysis above and the proposed strategy. The main parameters of the prototype are presented in Table I and the experiment platform is set up, which is shown in Fig.10.

TABLE I
PARAMETERS OF THE PROTOTYPE

Parameter	Symbol	Value
DC bus voltage	U_{DC}	$100V$
Switching frequency	f	$10kHz$
Stator resistance	R	0.8Ω
Number of Slots	N	12
Pole pairs	P	5
Rated speed	n	600rpm
Rated current	I_{phase}	2.4A
Flux linkage	Ψ_{md}	$0.03779W_b$

The platform consists of a DTP-PMSM, which is controlled by TMS320F28335DSP and two sets of driving boards based on insulated-gate bipolar transistor (IGBT). The load machine is connected to a resistive load on one side and the prototype on the other side. The sampling frequency of the current loop

is 10kHz, and 2kHz for the speed loop. The position signals are collected by an encoder.

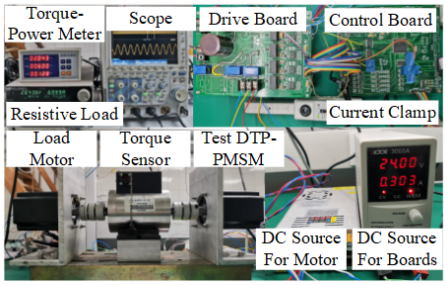

Fig.10 Experimental Platform

B. *Simulation Verification*

The simulation results are mainly utilized to verify the derivation of the voltage difference in Section IV and whether the proposed FTC algorithm can effectively compensate for the voltage difference in the faulty phase. The controller output voltage signals and the real winding voltages, in the faulty phase C_1 and the phase-to-phase voltage between B_1 and C_1 are compared under different conditions, including normal operation, OPF in phase C_1 without FTC, and OPF in phase C_1 with proposed FTC. The parameters in Table I are used in the simulation model. Since the actual voltages are processed by modulation strategies, they are chopped waves. This makes the waveform comparison unintuitive. So the FFT analysis is utilized in the voltage comparison, where the amplitude of the fundamental voltages are compared, as shown in Fig.11.

It can be seen from Fig.11 that after the OPF, the voltage difference will occur, both in the faulty phase and the related phase-to-phase voltage. It matches the analysis in Section IV. When no FTC scheme is utilized, the controller output voltage is larger than that when healthy but the actual voltage in the faulty phase reduces. A larger controller output is due to the regulation effect of the PI controller, but a smaller actual voltage shows that the control signal cannot be transmitted to the machine due to the OPF. And the proposed FTC with voltage compensation can successfully reduce the voltage difference according to Fig.11.

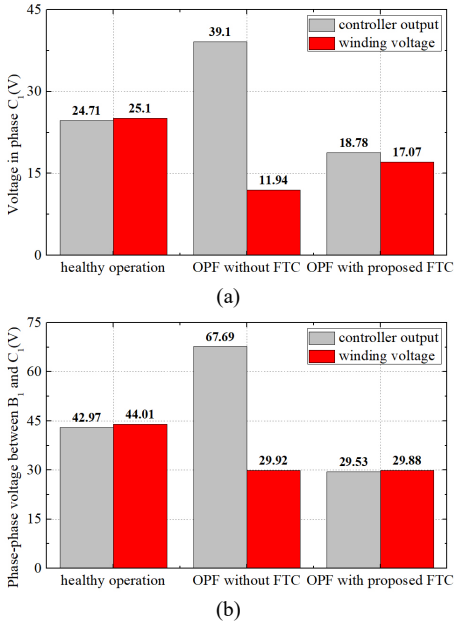

Fig.11 Comparison of controller output voltages and actual voltages. (a) u_{c1}. (b) u_{b1c1}

C. *Experimental Verification*

The proposed control scheme is investigated in the DTP-PMSM prototype as shown in Fig.10. Five operation conditions are compared in the experiments. They are 1) healthy operation; 2) OPF in phase C_1 without FTC; 3) OPF in phase C_1 with conventional 3-loop FTC based on virtual healthy model; 4) OPF in phase C_1 with proposed FTC without quasi-PR controller; 5) OPF in phase C_1 with proposed FTC. The conventional 3-loop FTC based on virtual healthy model can be designed according to Section III, part A by removing the z_2-axis and setting u_{z2ref} as 0. And the voltage compensation is used in 4) without a quasi-PR controller.

The parameters of the PI controllers remain the same to provide fair comparison under different operation conditions. The proportional gain of the PI controller for the current loop in d-q axes is k_{pq}=2.5, the integral gain is k_{iq}=0.1; For the current loop in z1-z2 axes, the proportional gain is k_{pz}=1, the integral gain is k_{iz}=0.1. The proportional gain of the PI controller for the speed loop is k_{ps}=0.008, the integral gain is k_{is}=0.006. As for the coefficients in the quasi-PR controller, the proportional element k_p is chosen as 2.5, the resonance coefficient k_r is chosen as 30 and the bandwidth ω_c is chosen as 6.28.

The phase currents are tested first and the speed is chosen as 600rpm. The waveforms are shown in Fig.12 and the FFT analysis of their fundamental components is shown in Fig.13.

To ensure the postfault operation of the prototype with

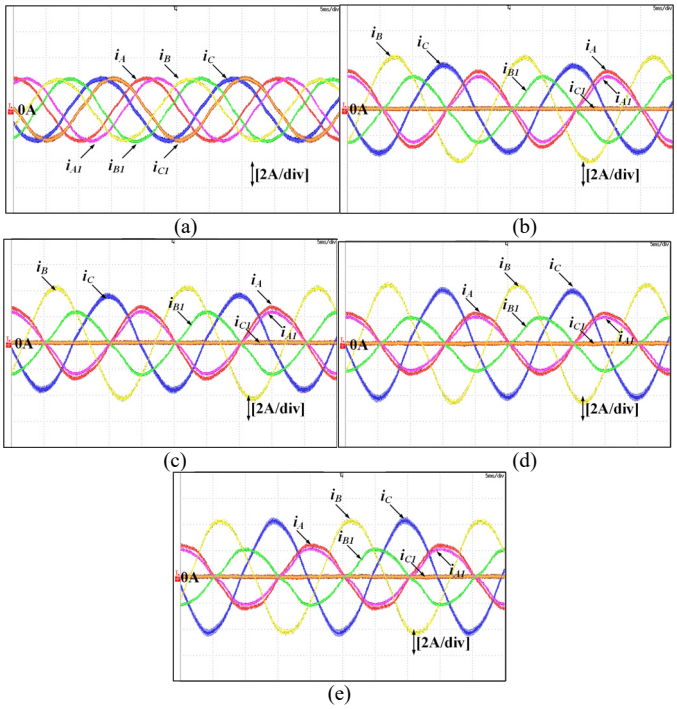

Fig.12 Phase current waveforms under different operation conditions. (a) healthy (b) OPF without FTC (c) OPF with conventional FTC (d) Proposed FTC without A-PR controller (e) Proposed FTC

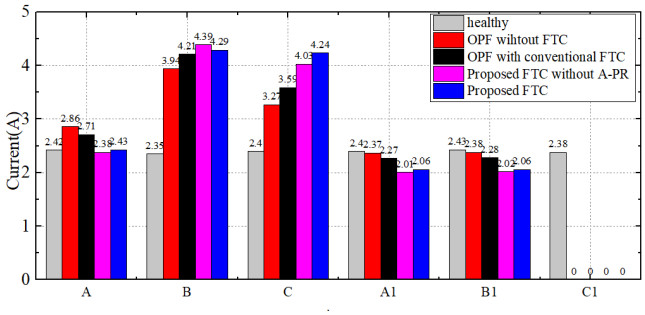

Fig.13 FFT analysis of the phase currents under different operation conditions

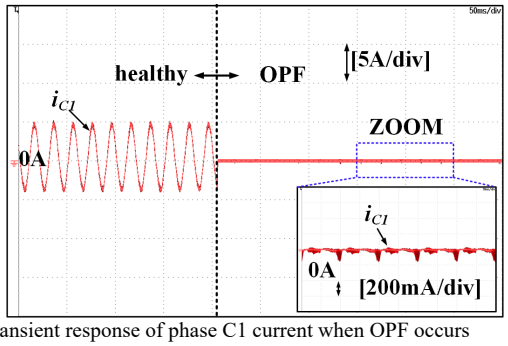

Fig.16 Transient response of phase C1 current when OPF occurs

minimum copper loss, the relationship among the phase current amplitudes should satisfy (12). The phase B current and phase C current should have the same amplitude and the amplitude is about 1.8 times of phase A current. And the phase A current should remain the same under postfault. According to Fig.12(a)~(c) and Fig.13, when operating under the traditional virtual healthy model-based FTC, the relationship in phase currents is not consistent with (12), for instance, though the error between i_B and i_C decreased compared to that without FTC, it is still not neglectable. It shows that the traditional FTC scheme cannot achieve its control target because of neglecting the voltage difference. When the voltage compensation is added in Fig.12(d), the error between the actual current and the theoretical value is reduced obviously. It proves the effectiveness of the voltage compensation. If the quasi-PR controller is also utilized, the quantitative relationship of each phase current as shown in Fig.12(e) and Fig.13 is basically the same as (12), achieving a further improvement compared to Fig.12(d).

The torque under different operation conditions is also compared. The torque waveforms are shown in Fig.14 and the relevant FFT analysis is shown in Fig.15. The experiments are done at the load torque of 1.35N·m and 600rpm. The results in Fig.15 show that the DC component of the torque remains unchanged under all circumstances. It shows that the main torque ripple component is 2nd torque ripple after the OPF occurs. The conventional FTC based on the virtual healthy model can reduce the torque ripple to a certain degree, from 0.31N·m to 0.24N·m. And the voltage compensation will halve the torque ripple compared to the conventional one. Finally, the proposed FTC with voltage compensation and quasi-PR controller can basically eliminate the 2nd torque ripple thus providing a smooth output torque.

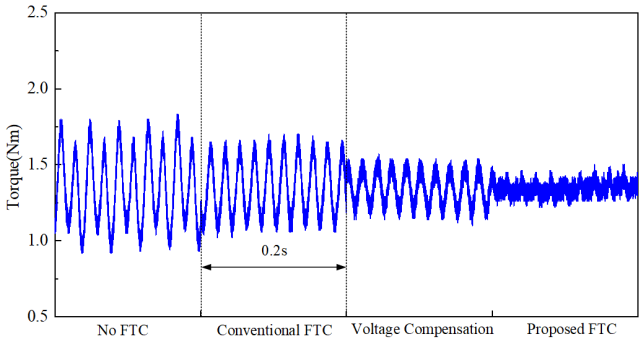

Fig.14 Torque waveforms under different operation conditions

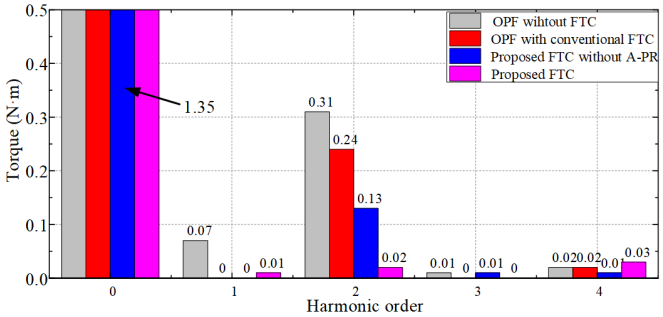

Fig.15 FFT analysis of the torque under different operation conditions

To test the effect of the antiparallel diodes, experiments are proposed. The transient response of the phase C_1 current when shutting down the power switches in phase C_1 by software can be shown in Fig.16. It shows that the current in the faulty phase, i_{c1}, exists and oscillates at 0A after the switches in phase C_1 are switched off due to the existence of the diodes. But the amplitude is less than 0.2A, which is minor compared to the phase currents.

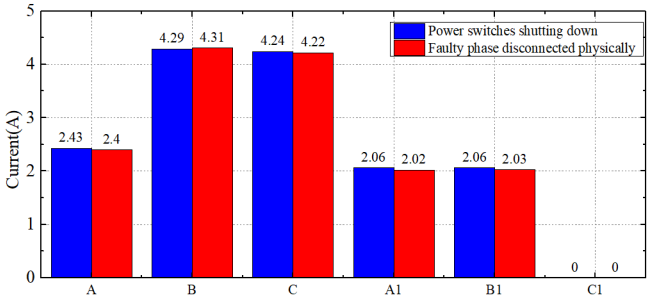

Fig.17 FFT analysis of the phase currents under proposed FTC scheme with different open-phase strategy

To analyze the effect of the antiparallel diodes on the proposed FTC scheme more comprehensively, phase C_1 is disconnected from the inverter physically to provide comparison. The diodes in phase C_1 will not operate and i_{c1} is always 0. The experiments are operated at the same working condition as that in Fig.12(e). The phase current waveforms are tested. The comparison of the FFT analysis between the diode conducting and diode non-conducting in the faulty phase is shown in Fig.17. According to the experiment results in Fig.17, the effect of the antiparallel diodes can be neglected in the proposed FTC scheme. The freewheeling current in the faulty phase under OPF can be used to extract the motor information, such as back EMF, but it will not affect the performance of the proposed FTC scheme.

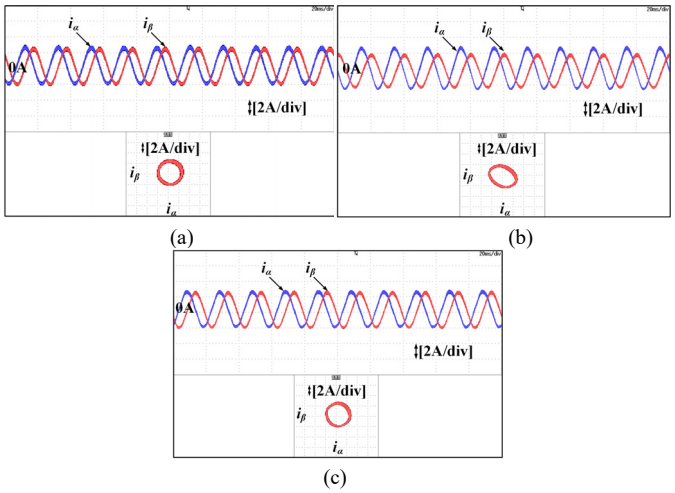

Fig.18 α-β axes waveforms under different operation conditions. (a) healthy (b) OPF with conventional FTC (c) Proposed FTC

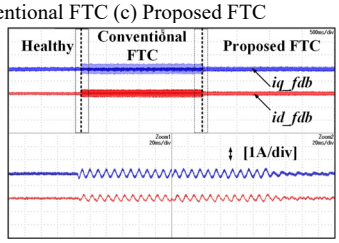

Fig.19 d-q axes waveforms under healthy operation and different FTC strategies

The experiments above show the effectiveness of the proposed strategy and its advantage on torque ripple suppression. The proposed controller is further tested then. According to (10), i_α, i_β should be symmetric under postfault operations to achieve a good fault-tolerant performance. And the corresponding Lissajous figure should be a circle. The α-β axes current and the Lissajous waves are shown in Fig.18 under healthy state, the conventional three-loop FTC and proposed FTC. And the waveforms of the d-q axes current under different operation conditions as shown in Fig.18 are shown in Fig.19. The α-β axes current and d-q axes current are derived from the Digital-to-Analog (DA) interface.

According to Fig.18(b), after the OPF in phase C_1, when the conventional FTC is proposed, there's an obvious difference between i_α and i_β, and the Lissajous figure is an ellipse instead of a circle. While after the proposed FTC, i_α and i_β are basically the same and the Lissajous figure is a circle, the same as that in Fig.18(a). The experimental results in Fig.19 show that the 3-loop conventional FTC strategy based on the virtual healthy model will not eliminate fluctuation in the d-q axes current waveforms and the proposed strategy will greatly reduce the current fluctuation in d-q axes, which can prove the effectiveness of the proposed strategy.

Since no iterative calculation is needed, the proposed strategy is promised to have a fast dynamic response. And it can be validated by testing the phase current response under sudden load change and speed change. The phase A current waveform of the dynamic response is shown in Fig.20. The waveform when speed changes from 400rpm to 600rpm, the rated speed, is shown in Fig.20(a) and it proved the good dynamic response. Fig.20(b) shows that the proposed strategy

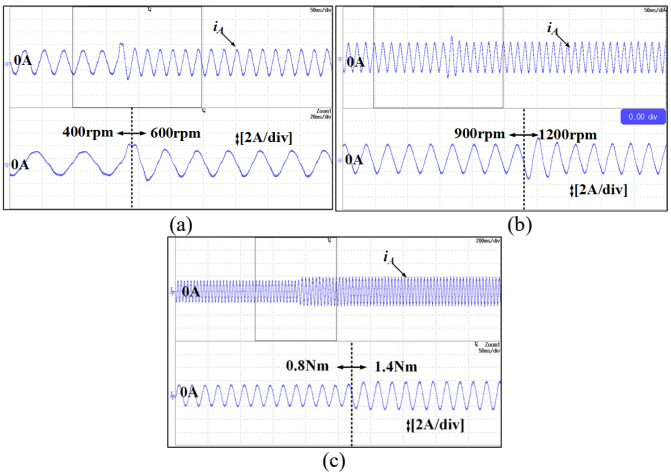

Fig.20 Transient response of phase A current (a) speed changing at normal range (b) speed changing at higher speed (c) load changing

still operates well and has good dynamic response at a higher speed when the speed changing from 900rpm to 1200rpm. The load change from 0.8Nm to 1.4 Nm is shown in Fig.20(c) with a speed of 600rpm. And the waveforms in Fig.20 prove the good dynamic performance in the proposed strategy.

VII. Conclusion

In this paper, an FTC strategy for OPF based on the virtual healthy model in DTP-PMSMs is proposed to suppress the torque ripple and reduce the copper loss. The proposed FTC scheme takes the voltage difference between the controller output voltage and actual winding voltages under OPF into consideration during the design. Voltage compensation and the quasi-PR controller are utilized to eliminate the torque distortion caused by the voltage difference. And the following conclusions can be drawn,

(1) The virtual healthy model is a promising modeling strategy to the DTP-PMSMs under OPF since the transformation matrix keeps unchanged and both the control scheme and the modulation scheme suitable for healthy DTP-PMSMs can still be applicable under postfault operations. Besides, only 3 current loops are needed in the virtual healthy model-based FTC compared to 4 current loops when healthy. And the sinusoidal current references are also derived to achieve minimum copper loss.

(2) the OPF will also interfere with the transmission of the controller output voltage signals. The voltage difference between the controller output voltage and actual winding voltages in OPF should also be considered in the virtual healthy model-based FTC schemes. The analysis shows that ignoring that voltage difference will induce the 2nd torque ripple component, as well as the change in fundamental component and 3rd harmonic components in phase currents.

(3) The proposed FTC scheme can successfully suppress the torque ripple caused by the voltage difference according to the theoretical analysis and experiments. The voltage compensation plays an important role in torque ripple suppression at low speeds while the

quasi-PR controller is essential when the speed is high. And the transient response is fast. The proposed controller will keep the system stable under different conditions. The effect of the antiparallel diode in the faulty phase will not affect the fault tolerant performance.

In conclusion, the presented method provides a solution to the high-performance postfault operation in DTP-PMSMs without significant change to the original controller or complex algorithms, improving the reliability of the overall system.

REFERENCES

[1] B. Shao *et al.*, "Improved Direct Torque Control Method for Dual-Three-Phase Permanent-Magnet Synchronous Machines With Back EMF Harmonics," *IEEE Transactions on Industrial Electronics,* vol. 68, no. 10, pp. 9319-9333, 2021.

[2] K. Yu and Z. Wang, "Improved Deadbeat Predictive Current Control of Dual Three-Phase Variable-Flux PMSM Drives with Composite Disturbance Observer," *IEEE Transactions on Power Electronics,* doi: 10.1109/TPEL.2022.3141375.

[3] W. Cao, B. C. Mecrow, G. J. Atkinson, J. W. Bennett, and D. J. Atkinson, "Overview of Electric Motor Technologies Used for More Electric Aircraft (MEA)," *IEEE Transactions on Industrial Electronics,* vol. 59, no. 9, pp. 3523-3531, 2012.

[4] Z. Huang, T. Yang, P. Giangrande, M. Galea, and P. Wheeler, "Technical Review of Dual Inverter Topologies for More Electric Aircraft Applications," *IEEE Transactions on Transportation Electrification,* doi: 10.1109/TTE.2021.3113606.

[5] X. Lang, T. Yang, Z. Wang, C. Wang, S. Bozhko, and P. Wheeler, "Fault Tolerant Control of Advanced Power Generation Center for More-Electric Aircraft Applications," *IEEE Transactions on Transportation Electrification,* doi: 10.1109/TTE.2021.3093506.

[6] F. Guo *et al.*, "An Overmodulation Algorithm With Neutral-Point Voltage Balancing for Three-Level Converters in High-Speed Aerospace Drives," *IEEE Transactions on Power Electronics,* vol. 37, no. 2, pp. 2021 - 2032, 2022.

[7] Y. Zuo, X. Zhu, X. Si, and C. H. T. Lee, "Fault-Tolerant Control for Multiple Open-Leg Faults in Open-End Winding Permanent Magnet Synchronous Motor System Based on Winding Reconnection," *IEEE Transactions on Power Electronics,* vol. 36, no. 5, pp. 6068-6078, 2021.

[8] X. Wang, Z. Wang, Z. Xu, M. Cheng, W. Wang, and Y. Hu, "Comprehensive Diagnosis and Tolerance Strategies for Electrical Faults and Sensor Faults in Dual Three-Phase PMSM Drives," *IEEE Transactions on Power Electronics,* vol. 34, no. 7, pp. 6669-6684, 2019.

[9] Y. Hu, Y. Feng, and X. Li, "Fault-tolerant Hybrid Current Control of Dual Three-phase PMSM with One Phase Open," *IEEE Journal of Emerging and Selected Topics in Power Electronics,* doi: 10.1109/JESTPE.2020.3032668.

[10] X. Wang, Z. Wang, M. Gu, D. Xiao, J. He, and A. Emadi, "Diagnosis-Free Self-Healing Scheme for Open-Circuit Faults in Dual Three-Phase PMSM Drives," *IEEE Transactions on Power Electronics,* vol. 35, no. 11, pp. 12053-12071, 2020.

[11] W. Wang, J. Zhang, M. Cheng, and S. Li, "Fault-Tolerant Control of Dual Three-Phase Permanent-Magnet Synchronous Machine Drives Under Open-Phase Faults," *IEEE Transactions on Power Electronics,* vol. 32, no. 3, pp. 2052-2063, 2017.

[12] S. Rubino, O. Dordevic, R. Bojoi, and E. Levi, "Modular Vector Control of Multi-Three-Phase Permanent Magnet Synchronous Motors," *IEEE Transactions on Industrial Electronics,* vol. 68, no. 10, pp. 9136-9147, 2021.

[13] Y. Luo and C. Liu, "Pre- and Post-Fault Tolerant Operation of a Six-Phase PMSM Motor Using FCS-MPC Without Controller Reconfiguration," *IEEE Transactions on Vehicular Technology,* vol. 68, no. 1, pp. 254-263, 2019.

[14] G. Feng, C. Lai, W. Peng, and N. C. Kar, "Decoupled Design of Fault Tolerant Control for Dual Three-phase IPMSM with Improved Memory Efficiency and Reduced Current RMS," *IEEE Transactions on Transportation Electrification,* doi: 10.1109/TTE.2021.3091468.

[15] Z. Liu, Z. Zheng, and Y. Li, "Enhancing Fault-Tolerant Ability of a Nine-Phase Induction Motor Drive System Using Fuzzy Logic Current Controllers," *IEEE Transactions on Energy Conversion,* vol. 32, no. 2, pp. 759-769, 2017.

[16] X. Wang, Z. Wang, Z. Xu, W. Wang, B. Wang, and Z. Zou, "Deadbeat Predictive Current Control-Based Fault-Tolerant Scheme for Dual Three-Phase PMSM Drives," *IEEE Journal of Emerging and Selected Topics in Power Electronics,* vol. 9, no. 2, pp. 1591-1604, 2021.

[17] B. Mirafzal, "Survey of Fault-Tolerance Techniques for Three-Phase Voltage Source Inverters," *IEEE Transactions on Industrial Electronics,* vol. 61, no. 10, pp. 5192-5202, 2014.

[18] J. D. Dasika and M. Saeedifard, "A Fault-Tolerant Strategy to Control the Matrix Converter Under an Open-Switch Failure," *IEEE Transactions on Industrial Electronics,* vol. 62, no. 2, pp. 680-691, 2015.

[19] X. Zhou, J. Sun, H. Li, M. Lu, and F. Zeng, "PMSM Open-Phase Fault-Tolerant Control Strategy Based on Four-Leg Inverter," *IEEE Transactions on Power Electronics,* vol. 35, no. 3, pp. 2799-2808, 2020.

[20] C. Sun, D. Sun, Z. Zheng, and H. Nian, "Simplified Model Predictive Control for Dual Inverter-Fed Open-Winding Permanent Magnet Synchronous Motor," *IEEE Transactions on Energy Conversion,* vol. 33, no. 4, pp. 1846-1854, 2018.

[21] J. Zhu, H. Bai, X. Wang, and X. Li, "Current Vector Control Strategy in a Dual-Winding Fault-Tolerant Permanent Magnet Motor Drive," *IEEE Transactions on Energy Conversion,* vol. 33, no. 4, pp. 2191-2199, 2018.

[22] A. G. Yepes, J. Doval-Gandoy, F. Baneira, and H. A. Toliyat, "Control Strategy for Dual Three-Phase Machines With Two Open Phases Providing Minimum Loss in the Full Torque Operation Range," *IEEE Transactions on Power Electronics,* vol. 33, no. 12, pp. 10044-10050, 2018.

[23] B. Tian, G. Mirzaeva, Q. An, L. Sun, and D. Semenov, "Fault-Tolerant Control of a Five-Phase Permanent Magnet Synchronous Motor for Industry Applications," *IEEE Transactions on Industry Applications,* vol. 54, no. 4, pp. 3943-3952, 2018.

[24] H. S. Che, M. J. Duran, E. Levi, M. Jones, W. Hew, and N. A. Rahim, "Postfault Operation of an Asymmetrical Six-Phase Induction Machine With Single and Two Isolated Neutral Points," *IEEE Transactions on Power Electronics,* vol. 29, no. 10, pp. 5406-5416, 2014.

[25] X. Wang, Z. Wang, M. He, Q. Zhou, X. Liu, and X. Meng, "Fault-Tolerant Control of Dual Three-Phase PMSM Drives With Minimized Copper Loss," *IEEE Transactions on Power Electronics,* vol. 36, no. 11, pp. 12938-12953, 2021.

[26] V. F. M. B. Melo, C. B. Jacobina, N. Rocha, and E. R. Braga-Filho, "Fault Tolerance Performance of Two Hybrid Six-Phase Drive Systems Under Single-Phase Open-Circuit Fault Operation," *IEEE Transactions on Industry Applications,* vol. 55, no. 3, pp. 2973-2983, 2019.

[27] G. Feng, C. Lai, W. Li, Y. Han, and N. Kar, "Computation-Efficient Solution to Open-phase Fault Tolerant Control of Dual Three-phase Interior PMSMs with Maximized Torque and Minimized Ripple," *IEEE Transactions on Power Electronics,* vol. 36, no. 4, pp. 4488 - 4499, 2021.

[28] I. González-Prieto, M. J. Duran, and F. J. Barrero, "Fault-Tolerant Control of Six-Phase Induction Motor Drives With Variable Current Injection," *IEEE Transactions on Power Electronics,* vol. 32, no. 10, pp. 7894-7903, 2017.

[29] I. Gonzalez-Prieto, M. J. Duran, F. Barrero, M. Bermudez, and H. Guzmán, "Impact of Postfault Flux Adaptation on Six-Phase Induction Motor Drives With Parallel Converters," *IEEE Transactions on Power Electronics,* vol. 32, no. 1, pp. 515-528, 2017.

[30] A. Mohammadpour, S. Mishra, and L. Parsa, "Fault-Tolerant Operation of Multiphase Permanent-Magnet Machines Using Iterative Learning Control," *IEEE Journal of Emerging and Selected Topics in Power Electronics,* vol. 2, no. 2, pp. 201-211, 2014.

[31] F. Baudart, B. Dehez, E. Matagne, D. Telteu-Nedelcu, P. Alexandre, and F. Labrique, "Torque Control Strategy of Polyphase Permanent-Magnet Synchronous Machines With Minimal Controller Reconfiguration Under Open-Circuit Fault of One Phase," *IEEE Transactions on Industrial Electronics,* vol. 59, no. 6, pp. 2632-2644, 2012.

[32] G. Feng, C. Lai, W. Li, J. Tjong, and N. C. Kar, "Open-Phase Fault Modeling and Optimized Fault-Tolerant Control of Dual Three-Phase Permanent Magnet Synchronous Machines," *IEEE Transactions on Power Electronics,* vol. 34, no. 11, pp. 11116-11127, 2019.

[33] M. Bermudez, I. Gonzalez-Prieto, F. Barrero, H. Guzman, M. J. Duran, and X. Kestelyn, "Open-Phase Fault-Tolerant Direct Torque Control Technique for Five-Phase Induction Motor Drives," *IEEE Transactions on Industrial Electronics,* vol. 64, no. 2, pp. 902-911, 2017.

[34] H. Guzman, F. Barrero, and M. J. Duran, "IGBT-Gating Failure Effect on a Fault-Tolerant Predictive Current-Controlled Five-Phase Induction Motor Drive," *IEEE Transactions on Industrial Electronics,* vol. 62, no. 1, pp. 15-20, 2015.

[35] B. Tian, M. Molinas, Q. An, B. Zhou, and J. Wei, "Freewheeling Current-Based Sensorless Field-Oriented Control of Five-Phase Permanent Magnet Synchronous Motors Under Insulated Gate Bipolar Transistor Failures of a Single Phase," *IEEE Transactions on Industrial Electronics,* vol. 69, no. 1, pp. 213-224, 2022.

[36] Z. Yifan and T. A. Lipo, "Space vector PWM control of dual three-phase induction machine using vector space decomposition," *IEEE Transactions on Industry Applications,* vol. 31, no. 5, pp. 1100-1109, 1995.

[37] Y. Xu, B. Zheng, G. Wang, H. Yan, and J. Zou, "Current Harmonic Suppression in Dual Three-Phase Permanent Magnet Synchronous Machine With Extended State Observer," *IEEE Transactions on Power Electronics,* vol. 35, no. 11, pp. 12166-12180, 2020.

[38] X. Wang, Z. Wang, M. Cheng, and Y. Hu, "Remedial Strategies of T-NPC Three-Level Asymmetric Six-Phase PMSM Drives Based on SVM-DTC," *IEEE Transactions on Industrial Electronics,* vol. 64, no. 9, pp. 6841-6853, 2017.

[39] T. Qiu, X. Wen, and F. Zhao, "Adaptive-Linear-Neuron-Based Dead-Time Effects Compensation Scheme for PMSM Drives," *IEEE Transactions on Power Electronics,* vol. 31, no. 3, pp. 2530-2538, 2016.

[40] B. Zheng, Z. Jibin, Y. Xu, X. Lang, and G. Yu, "Torque Ripple Suppression based on Optimal Harmonic Current Injection in Dual Three-Phase PMSMs under Magnetic Saturation," *IEEE Transactions on Industrial Electronics,* vol. 69, no. 6, pp. 5398 - 5408, 2022.

[41] L. Yan *et al.*, "Multiple Synchronous Reference Frame Current Harmonic Regulation of Dual Three Phase PMSM with Enhanced Dynamic Performance and System Stability," *IEEE Transactions on Industrial Electronics,* doi: 10.1109/TIE.2021.3116553.